A&A 624, A52 (2019)
https://doi.org/10.1051/0004-6361/201834946

Astronomy & Astrophysics

Multi-wavelength torus–jet model for Sagittarius A*

F. H. Vincent[1], M. A. Abramowicz[2,3,4], A. A. Zdziarski[2], M. Wielgus[5,6], T. Paumard[1], G. Perrin[1], and O. Straub[7,1]

[1] LESIA, Observatoire de Paris, PSL Research University, CNRS, Sorbonne Universités, UPMC Univ. Paris 06, Univ. Paris Diderot, Sorbonne Paris Cité, 5 place Jules Janssen, 92195 Meudon, France
e-mail: frederic.vincent@obspm.fr
[2] Nicolaus Copernicus Astronomical Center, Polish Academy of Sciences, Bartycka 18, 00-716 Warszawa, Poland
[3] Physics Department, Gothenburg University, 412-96 Gothenborg, Sweden
[4] Physics Department, Silesian University of Opava, Czech Republic
[5] Harvard-Smithsonian Center for Astrophysics, 60 Garden St., Cambridge, MA 02138, USA
[6] Black Hole Initiative at Harvard University, 20 Garden St., Cambridge, MA 02138, USA
[7] Max Planck Institute for Extraterrestrial Physics, Giessenbachstr. 1, 85748 Garching, Germany

Received 21 December 2018 / Accepted 4 February 2019

ABSTRACT

Context. The properties of the accretion/ejection flow surrounding the supermassive central black hole of the Galaxy Sgr A* will be scrutinized by the new-generation instrument GRAVITY and the Event Horizon Telescope (EHT). Developing fast, robust, and simple models of such flows is therefore important and very timely.
Aims. We want to model the quiescent emission of Sgr A* from radio to mid-infrared wavelengths, using thermal and nonthermal synchrotron. The radiation is emitted by the overlay of a magnetized compact torus close to the black hole, and a large-scale magnetized jet. We compare model spectra and images to the multi-wavelength observable constraints available to date. We simulate EHT observations at 1.3 mm of the best-fit model for different inclinations.
methods. We use a simple analytic description for the geometry of the torus and jet. We model their emission by thermal synchrotron and κ-distribution synchrotron, respectively. We use relativistic ray tracing to compute simulated spectra and images, restricting our analysis to the Schwarzschild (zero spin) case. A best-fit is found by adjusting the simulated spectra to the latest observed data, and we check the consistency of our spectral best fits with the radio-image sizes and infrared spectral index constraints. We use the open-source `eht-imaging` library to generate EHT-reconstructed images.
Results. We find perfect spectral fit ($\chi^2_{\rm red} \approx 1$) both for nearly face-on and nearly edge-on views. These best fits give parameter values very close to those found by the most recent numerical simulations, which are much more complex than our model. The intrinsic radio size of Sgr A* is found to be in reasonable agreement with the centimetric observed constraints. Our best-fit infrared spectral index is in perfect agreement with the latest constraints. Our emission region at 1.3 mm, although larger than the early-EHT Gaussian best fit, does contain bright features at the $\lesssim$40 μas scale. EHT-reconstructed images show that torus/jet-specific features persist after the reconstruction procedure, and that these features are sensitive to inclination.
Conclusions. The main interest of our model is to provide a simple and fast model of the quiescent state of Sgr A*, which gives extremely similar results to those of state-of-the-art numerical simulations. Our model is easy to use and we publish all the material necessary to reproduce our spectra and images, meaning that anyone interested can use our results relatively straightforwardly. We hope that such a public tool will be useful in the context of the recent and near-future GRAVITY and EHT results.

Key words. Galaxy: center – accretion, accretion disks – black hole physics – relativistic processes

1. Introduction

The supermassive black hole at the center of our Galaxy, Sgr A*, is the best target for studying the vicinity of a black hole at high angular resolution. With a mass of $\approx 4 \times 10^6\, M_\odot$ at a distance of $\approx$8 kpc (Ghez et al. 2008; Gillessen et al. 2009), the angular size of this object (more precisely, of the black hole shadow, Falcke et al. 2000a) is of $\approx$50 μas, making it the biggest black hole in the Universe on sky. It is therefore of particular importance to study the properties of the accretion flow surrounding this object, and compare them with observable constraints.

The study of Sgr A* is entering a new era with the advent of $\approx$10−30 μas-scale observations that are starting to be delivered by the new-generation instruments GRAVITY (Gravity Collaboration 2017, 2018a) and the Event Horizon Telescope (EHT; Doeleman et al. 2009). These instruments will, among other objectives, allow for a much more precise understanding of the physics of the accreted gas close to the black hole. In this perspective, modeling the electromagnetic radiation emerging from this accretion flow is important.

In this study, we focus on the quiescent emission of Sgr A*, when the source does not show outbursts or flares of radiation (see e.g. Dodds-Eden et al. 2011, and references therein). For a complete review of Sgr A* emission in the quiescent and flaring states, see Genzel et al. (2010). The quiescent radiation emitted in the region around Sgr A* can be broadly divided into the following spectra.

– The radio spectrum (1−100 GHz, 3 mm–30 cm) is mainly due to nonthermal synchrotron (Yuan et al. 2003) emitted far from the black hole. The observed size is dominated by the scattering effects (Bower et al. 2006; Falcke et al. 2009). The radio counterpart of Sgr A* has been studied for decades by means of Very Long Baseline Interferometry (VLBI; Alberdi et al. 1993; Bower et al. 2014).

– The millimeter spectrum (100 GHz–1 THz, 0.3 mm–3 mm) is due to a mixture of thermal and nonthermal synchrotron (Yuan et al. 2003) emitted very close to the black hole (inner few tens to hundreds of μas, Doeleman et al. 2008). The EHT observes in this range at 1.3 mm, with future plans to enable observations at 0.86 mm. Advanced scattering mitigation algorithms were recently developed to enable Sgr A* intrinsic imaging in the millimeter range (Johnson 2016);
– The infrared spectrum (between $\approx$1 and $\approx$10 μm) is mainly due to nonthermal synchrotron radiation (Yuan et al. 2003; Witzel et al. 2018) emitted in the inner regions. GRAVITY observes in this range at 2.2 μm.
– The X-ray spectrum (2−10 keV) is mainly due to thermal bremsstrahlung emitted at large scales in the central arcsecond (Quataert 2002), with the addition of a small (<20%) contribution due to Compton scattering arising from the inner regions (Wang et al. 2013).

Modeling Sgr A* accretion/ejection flow in the aim of accounting for part or all of these emission processes has been a very intense area of research in the past decades. Our Galactic center is an extreme case of a low-luminosity galactic nucleus, radiating at $\approx 10^{-8}$ of the Eddington level. As such, Sgr A* is a prototype for the class of hot accretion flows, for which most of the energy is advected inwards and/or ejected as outflows, rather than radiated away (see Yuan & Narayan 2014, for a review). It is practical to divide publications on this subject into those models that are analytical, and those using numerical simulations (general relativistic magnetohydrodynamics simulations, or GRMHD). Analytical studies can themselves be divided into those dedicated to studying the emission of geometrically thick hot disks, known as radiatively inefficient accretion flows (RIAF, Narayan et al. 1995; Özel et al. 2000; Yuan et al. 2003; Broderick et al. 2016), or ionized tori (Rees 1982; Straub et al. 2012; Vincent et al. 2015), and those studying the emission of a large-scale jet (Falcke et al. 1993; Falcke & Markoff 2000; Markoff et al. 2001). GRMHD simulations of Sgr A* emerged a decade ago (Mościbrodzka et al. 2009; Dexter et al. 2010; Shcherbakov et al. 2012; Dibi et al. 2012), and soon became an extremely active field with the perspective of the EHT observations (Ressler et al. 2017; Gold et al. 2017; Chael et al. 2018; Jiménez-Rosales & Dexter 2018; Davelaar et al. 2018, citing only the most recent works; see many other references therein).

Although GRMHD models become more and more common with time, it is still important to devote efforts to the development and use of analytic models. Indeed, analytic descriptions have the advantage of their simplicity: a few carefully chosen parameters, with clear physical meaning, describe only those physical effects that are considered by the authors to be relevant to account for observable effects. Such a framework circumvents the great difficulty of discriminating the putative numerical artefacts (typically linked to a particular initial or boundary condition) that might impact the results of GRMHD simulations. Moreover, analytic models are much faster, and are therefore well adapted to scan parameter spaces, paving the way for future, more demanding GRMHD studies. In particular, analytical models are well adapted for studying nonstandard scenarios, such as alternative compact objects (Vincent et al. 2016b,a; Lamy et al. 2018).

This article is devoted to expanding our past studies that aimed at accounting for the emission of the surroundings of Sgr A* with a simple magnetized torus in the few tens of gravitational radii from the black hole. This series of analyses started with Straub et al. (2012) and Vincent et al. (2015), in which we showed that we could fit the millimeter spectrum of Sgr A* well, but were not able to account for the radio data, given that larger-scale emission is needed for that. As a consequence, we consider in this article the addition of a large-scale jet, on top of the same magnetized torus as introduced in our past studies. We note that a jet has already been coupled to an advection-dominated hot flow by Yuan et al. (2002), although not with ray tracing as we do here, which does not allow for the aspect of the millimetric images to be predicted. The existence of a jet at the Galactic center is supported by the fact that such outflows have been detected in other low-luminosity AGNs (Falcke et al. 2000b; Bietenholz et al. 2000). Moreover, numerical simulations demonstrate the natural link between hot accretion flows and outflows (Yuan & Narayan 2014). However, no clear observational proof of the existence of a jet at the Galactic center has yet been obtained, and recent work by Issaoun et al. (2019) favors either disk-dominated models or face-on jet-dominated models as more likely to explain 3.5 mm spatially resolved emission from the Galactic center. The presence of a jet at the Galactic center is thus still an open question.

Our goal is to fit the radio to infrared spectrum of Sgr A*. We do not yet aim at accounting for the X-ray emission because this would ask for still larger-scale simulations to take into account the thermal bremsstrahlung that accounts for most of the quiescent X rays. Also, our prime interest for later use of this model is the interpretation of GRAVITY and EHT data, therefore X rays are not our primary target.

We insist on the fact that our model is fully open-source, and readily available to be used by other authors without significant effort. Appendix C gives the necessary and sufficient information to be able to generate most of the numerical results presented in this article.

Section 2 presents the analytic torus+jet model that we use, Sect. 3 gives our results in terms of best-fit spectra and images, Sect. 4 presents examples of synthetic reconstructions of model images with a numerical EHT array, and Sect. 5 discusses our conclusions and perspectives.

2. Torus-jet model

Throughout, the spacetime is assumed to be described by the Kerr metric in Boyer-Lindquist (t, r, θ, φ) coordinates, describing a rotating black hole with mass M and dimensionless spin parameter a. In this article, we are not interested in the (small) effect of the spin parameter, and keep $a = 0$ (Schwarzschild metric) throughout, although our model is fully valid for any spin value. The cylindrical radius is defined by $\rho = r \sin\theta$ (ρ is never a density in this article, it always labels the cylindrical radius). The height is defined by $z = r \cos\theta$.

We describe two structures below that aim at being the sources of the synchrotron radiation emitted around Sgr A*:
– A magnetized torus which gives a reasonable approximation of a snapshot of a realistic accreting geometrically thick accretion flow. This torus emits the thermal synchrotron responsible for the millimeter peak of Sgr A*.
– A jet sheath, modeled as simply as possible to capture only the crucial features of a realistic ejection flow. This jet emits a mixed thermal/nonthermal synchrotron radiation that allows us to reproduce the radio spectrum of Sgr A*, as well as the mid- and far-infrared data.

We note that we do not consider the X-ray emission (which needs bremsstrahlung and Comptonization) in this article. This is postponed to a later study. This choice is dictated by our prime

interest in the infrared and millimeter instruments, GRAVITY and the EHT.

2.1. Torus model and its thermal synchrotron emission

The torus structure exactly follows the description of Vincent et al. (2015), to which we refer for further details. In this article, we consider a chaotic magnetic field (i.e., isotropized, as compared to the toroidal field of Komissarov 2006), given that Vincent et al. (2015) have shown that the magnetic field directionality has no impact on the spectral observables.

For completeness, we reiterate here the major features of this torus model. We consider a circularly rotating perfect fluid described by a constant angular momentum $\ell = -u_\varphi/u_\mathrm{t}$, where $\boldsymbol{u}$ is the 4-velocity of the fluid. The conservation of stress-energy leads to

$$\frac{\nabla_\mu p}{p+\epsilon} = -\nabla_\mu \ln(-u_\mathrm{t}), \tag{1}$$

where p is the fluid pressure and ϵ is the fluid total energy density. The constant-pressure surfaces are therefore the same as the isocontours of the potential $\mathcal{W} = \ln(-u_\mathrm{t})$. This leads to a toroidal shape that is fully defined by the choice of ℓ together with the choice of the inner radius r_in of the torus. The pressure is linked to enthalpy h by means of the polytropic equation of state $p = \kappa h^k$, where k is the polytropic index. The electron number density is then deduced from the enthalpy profile and can be shown to be fully characterized by the potential $\mathcal{W}$ and a chosen averaged number density at the torus center $\langle n_\mathrm{e}\rangle^{\mathrm{T\ cen}}$ (see Vincent et al. 2015, for details). Hereafter, a superscript T labels a torus quantity, while a superscript J labels a jet quantity. The magnetic field is found by choosing the magnetization parameter σ (see Eq. (6)). Finally, the electron temperature T_e^T varies as $\left(\langle n_\mathrm{e}\rangle^\mathrm{T}\right)^{k-1}$, with a scaling defined by the central temperature, $T_\mathrm{e}^{\mathrm{T\ cen}}$, which is a free parameter of the model. We refer the reader to Fig. 2 of Vincent et al. (2015) and Fig. 2 of Straub et al. (2012) for descriptions of the density and temperature profiles of the torus, respectively, as well as a comparison with the RIAF model. We stress that our torus is very compact and restricted to the inner ≈15 gravitational units.

We consider a population of thermal electrons at any point inside the torus, with a number density distribution satisfying

$$n_\mathrm{e}^\mathrm{ther}(\gamma) = \frac{\langle n_\mathrm{e}\rangle^\mathrm{T}}{\theta_\mathrm{e}} \frac{\gamma(\gamma^2-1)^{1/2}}{K_2(1/\theta_\mathrm{e})} e^{-\gamma/\theta_\mathrm{e}}, \tag{2}$$

where $\langle n_\mathrm{e}\rangle^\mathrm{T}$ is the energy-averaged electron number density in the torus, γ is the Lorentz factor of the electrons, $\theta_\mathrm{e} = kT_\mathrm{e}^\mathrm{T}/m_\mathrm{e}c^2$ is the dimensionless electron temperature (k is the Boltzmann constant, c the velocity of light), and K_2 is a modified Bessel function of the second kind. We remind the reader that the averaged number density $\langle n_\mathrm{e}\rangle^\mathrm{T}$ and temperature T_e^T are analytically known at any point of the torus.

The thermal synchrotron emission and absorption coefficients are different from Vincent et al. (2015). Here, we consider the formula provided by Pandya et al. (2016), in their Eq. (31), while Vincent et al. (2015) consider the formula of Wardziński & Zdziarski (2000). This change is made for consistency with the jet emission, which is taken from Pandya et al. (2016). The thermal synchrotron emission coefficient (in units of erg s^{-1} cm^{-3} ster^{-1} Hz^{-1}) reads

$$j_\nu^\mathrm{ther} = \frac{\langle n_\mathrm{e}\rangle^\mathrm{T} e^2 \nu_\mathrm{c}}{c} e^{-X^{1/3}} \frac{\sqrt{2}\pi}{27} \sin\theta_B (X^{1/2} + 2^{11/12} X^{1/6})^2, \tag{3}$$

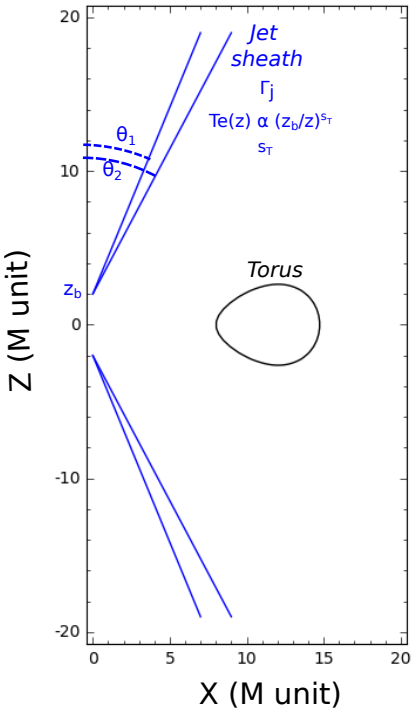

Fig. 1. Scheme of the torus-jet model. The jet is parametrized by the angles θ_1 and θ_2 that describe the angular opening of the radiation-emitting sheath, by the base height z_b, the constant Lorentz factor Γ_j, and the temperature power-law index s_T. The jet is symmetrical with respect to the equatorial plane, and axisymmetric.

where $X = \nu/\nu_\mathrm{s}$, $\nu_\mathrm{s} = 2/9\,\nu_\mathrm{c}\,\theta_e^2\,\sin\theta_B$, and $\nu_\mathrm{c} = e\,B/(2\pi\,m_\mathrm{e}\,c)$ is the cyclotron frequency, with e being the electron charge, m_e their mass, B the magnetic field magnitude, and θ_B is the angle between the magnetic field direction and the direction of photon emission (over which the emission is averaged). The absorption coefficient (in units of cm^{-1}) is found from Kirchhoff's law, $\alpha_\nu^\mathrm{ther} = j_\nu^\mathrm{ther}/B_\nu$, where B_ν is the Planck blackbody function.

2.2. Jet model and its synchrotron emission

We want to keep our analytical jet model as simple as possible, and close to the recent disk-jet GRMHD simulations obtained for Sgr A* by Mościbrodzka & Falcke (2013), and Davelaar et al. (2018). These simulations show in particular that the radiation from the jet actually comes from a narrow sheath, while most of the interior of the jet (the spine) is empty of matter and therefore does not contribute to the emission. This finding was confirmed by Ressler et al. (2017). We therefore consider the model illustrated in Fig. 1. The emitting region is assumed to be defined by a thin layer in between two conical surfaces defined by the angles θ_1 and θ_2, and truncated at the jet base height z_b. The bulk Lorentz factor, as measured by the zero-angular-momentum observer (ZAMO[1]), is assumed constant at Γ_j. The acceleration zone is therefore discarded in this simple model.

Following Davelaar et al. (2018) we consider a population of electrons at any point inside the jet sheath satisfying a

[1] We remind the reader that the ZAMO is defined in Boyer-Lindquist coordinates by having zero angular momentum, $u_\varphi = 0$, at some fixed r in the equatorial plane $\theta = \pi/2$. This fully fixes the ZAMO 4-velocity. In the Schwarzschild metric, such an observer is simply static. In the Kerr metric with nonzero spin, the ZAMO has a varying φ coordinate due to frame-dragging.

κ-distribution

$$n_{\rm e}^{\kappa-{\rm distrib}}(\gamma) = N\,\gamma(\gamma^2-1)^{1/2}\left(1+\frac{\gamma-1}{\kappa\theta_{\rm e}}\right)^{-(\kappa+1)}, \tag{4}$$

where N is a normalization factor depending on the averaged electron number density in the jet, $\langle n_{\rm e}\rangle^{\rm J}$, and the dimensionless temperature $\theta_{\rm e}$ (N is defined by $\int_\gamma n_{\rm e}^{\kappa-{\rm distrib}}(\gamma){\rm d}\gamma = \langle n_{\rm e}\rangle^{\rm J}$), γ is the Lorentz factor of the electrons, and κ is a parameter. This distribution smoothly connects a thermal distribution for small electron Lorentz factor to a power-law distribution with power-law index $p = \kappa - 1$ at high electron Lorentz factor. We refer to Fig. 1 of Pandya et al. (2016) for an illustration of this distribution (note that the thermal/power-law transition takes place close to the peak of the distribution; this is different from the thermal+power-law-tail spectrum of the hard state of Cygnus X−1 as discussed in McConnell et al. 2002).

The averaged electron number density varies with the altitude z. By the conservation of mass, this quantity must scale as $\rho(z)^{-2}$ so that we can write

$$\langle n_{\rm e}\rangle^{\rm J}(z) = \langle n_{\rm e}\rangle^{\rm J\ base}\,\frac{\rho(z_b)^2}{\rho(z)^2}, \tag{5}$$

where $\langle n_{\rm e}\rangle^{\rm J\ base}$ is the electron number density at the base of the jet, which is a parameter of the model. To obtain this expression, we assume that the jet matter flows across surfaces of area $\propto\rho(z)^2$, meaning that we consider the full jet (spine+sheath) for the mass conservation, while we consider only the sheath for the emission. This is reasonable given that the number density in the spine is typically extremely low (Mościbrodzka & Falcke 2013).

The magnetic field magnitude follows from the specification of the magnetization parameter σ

$$\frac{B(z)^2}{4\pi} = \sigma\, m_{\rm p} c^2\,\langle n_{\rm e}\rangle^{\rm J}(z), \tag{6}$$

where $m_{\rm p}$ is the proton mass. This means that the magnetic field will approximately scale like $1/r$.

The temperature of the electrons at the base of the jet, $T_{\rm e}^{\rm J\ base}$, is a parameter of the model. We are therefore free to prescribe the profile of temperature with altitude. To justify our choice, let us reiterate that the standard isothermal jet model of Blandford & Königl (1979) produces a flat radio spectrum. For Sgr A*, Fig. 2 shows that the radio spectral data are not exactly flat: more flux is needed at higher frequencies (closer to the black hole), rather than at lower frequencies (further from the black hole). To obtain this behavior, we consider a nonisothermal model such that the temperature decreases with altitude following a power law

$$T_{\rm e}^{\rm J}(z) = T_{\rm e}^{\rm J\ base}\left(\frac{z_{\rm b}}{z}\right)^{s_{\rm T}}, \tag{7}$$

where the temperature slope $s_{\rm T}$ is a parameter. A value of $s_{\rm T} = 0$ would lead to an isothermal jet model close to Blandford & Königl (1979). We consider values $0 \le s_{\rm T} \le 1$.

Our goal is to ray trace this model and therefore we need to properly define the 4-velocity of the ejected gas at every point inside the jet, which is needed to compute redshift effects during the ray tracing. The Lorentz factor Γ_j being measured by the ZAMO with 4-velocity $\boldsymbol{u}_{\rm ZAMO}$, the 4-velocity of the jet particles can be written

$$\boldsymbol{u}_{\rm jet} = \Gamma_j\,(\boldsymbol{u}_{\rm ZAMO} + \boldsymbol{V}), \tag{8}$$

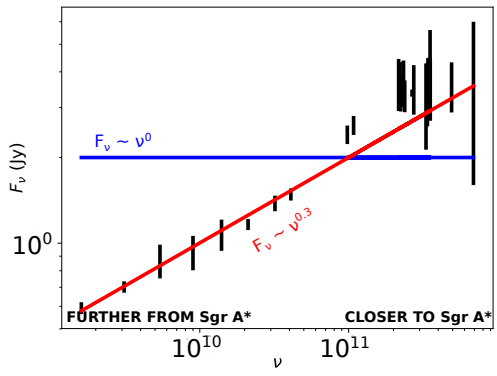

Fig. 2. The radio to millimeter spectrum of Sgr A* (black error bars are as in Fig. 3). The blue horizontal line shows the spectrum produced by an isothermal jet. The red line shows what is needed by the data.

where $\boldsymbol{V} = (V^t = 0, V^r, V^\theta, V^\varphi = 0)$ is the jet velocity as measured by the ZAMO, and can be seen as the usual 3-velocity of the jet. Here, it has only two nonzero components due to the axisymmetry. This jet velocity can be written easily at the external and internal sheath surfaces (respectively defined by the angles θ_1 and θ_2)

$$\boldsymbol{V} = V\left(\sin\theta_k\,\boldsymbol{e}_\rho + \cos\theta_k\,\boldsymbol{e}_z\right), \tag{9}$$

where $\boldsymbol{e}_\rho$ and $\boldsymbol{e}_z$ are unit vectors, $V = \sqrt{\Gamma_j^2-1}/\Gamma_j$ is the jet velocity in units of the speed of light, and the angle $\theta_{\rm k}$ can be θ_1 or θ_2. The velocity at any point inside the sheath, defined by an angle with the $\boldsymbol{e}_z$ direction equal to $\theta_2 < \theta < \theta_1$, can then be easily interpolated linearly between θ_1 and θ_2.

The synchrotron emission and absorption coefficients for the κ-distribution electrons are taken from Eqs. (35)–(41) of Pandya et al. (2016), averaged over the angle θ_B between the magnetic field direction and the direction of emission. The low- and high-frequency dimensionless emission coefficients, as well as the bridging emission coefficient, read

$$\begin{aligned}
\mathcal{J}_\nu^{\rm low} &= X_\kappa^{1/3}\sin\theta_B\,\frac{4\pi\,\Gamma(\kappa-4/3)}{3^{7/3}\,\Gamma(\kappa-2)}, \\
\mathcal{J}_\nu^{\rm high} &= X_\kappa^{-(\kappa-2)/2}\sin\theta_B\,3^{(\kappa-1)/2} \\
&\quad\times\frac{(\kappa-2)(\kappa-1)}{4}\,\Gamma(\kappa/4-1/3)\Gamma(\kappa/4+4/3), \\
j_\nu^{\kappa-{\rm distrib}} &= \frac{\langle n_{\rm e}\rangle^{\rm J}\,e^2\,\nu_{\rm c}}{c}\left[\left(\mathcal{J}_\nu^{\rm low}\right)^{-x_j}+\left(\mathcal{J}_\nu^{\rm high}\right)^{-x_j}\right]^{-1/x_j},
\end{aligned} \tag{10}$$

where $X_\kappa = \nu/(\nu_{\rm c}(\theta_{\rm e}\kappa)^2\sin\theta_B)$, Γ is the gamma function, and $x_j = 3\,\kappa^{-3/2}$. This fit is correct for $3 \le \kappa \le 7$. Similarly, the absorption coefficient is given by

$$\begin{aligned}
\mathcal{A}_\nu^{\rm low} &= X_\kappa^{-2/3}\,3^{1/6}\,\frac{10}{41} \\
&\quad\times\frac{2\pi}{(\theta_{\rm e}\kappa)^{10/3-\kappa}}\,\frac{(\kappa-2)(\kappa-1)\kappa}{3\kappa-1}\,\Gamma(5/3) \\
&\quad\times{}_2F_1(\kappa-1/3,\kappa+1;\kappa+2/3;-\kappa\theta_{\rm e}), \\
\mathcal{A}_\nu^{\rm high} &= X_\kappa^{-(1+\kappa)/2}\,\frac{\pi^{3/2}}{3}\,\frac{(\kappa-2)(\kappa-1)\kappa}{(\theta_{\rm e}\kappa)^3} \\
&\quad\times\left[\frac{2\,\Gamma(2+\kappa/2)}{2+\kappa}-1\right]\left[\left(\frac{3}{\kappa}\right)^{19/4}+\frac{3}{5}\right], \\
\alpha_\nu^{\kappa-{\rm distrib}} &= \frac{\langle n_{\rm e}\rangle^{\rm J}\,e^2}{\nu\,m_{\rm e}\,c}\left[\left(\mathcal{A}_\nu^{\rm low}\right)^{-x_\alpha}+\left(\mathcal{A}_\nu^{\rm high}\right)^{-x_\alpha}\right]^{-1/x_\alpha},
\end{aligned} \tag{11}$$

Table 1. Torus+jet model best-fit parameters at inclination $i = 20°$.

Parameter		Value
Black hole		
Mass ($M_\odot$)	M	4.1×10^6
Distance (kpc)	D	8.1
Spin	a	0
Inclination (°)	i	20
Torus		
Angular momentum (GM/c^3)	ℓ	4
Inner radius (GM/c^2)	$r_{\rm in}$	**8**
Polytropic index	k	5/3
Central density (cm^{-3})	$\langle n_{\rm e}\rangle^{\rm T\ cen}$	$\mathbf{1.2 \times 10^9}$
Central temperature (K)	$T_{\rm e}^{\rm T\ cen}$	$\mathbf{7 \times 10^9}$
	$\Theta_{\rm e}^{\rm T\ cen}$	1.2
Magnetization parameter	$\sigma^{\rm T}$	0.002
Jet		
Inner opening angle (°)	θ_1	20
Outer opening angle (°)	θ_2	$\theta_1 + 3.5$
Jet base height ($GM\,c^{-2}$)	z_b	2
Bulk Lorentz factor	Γ_j	1.15
Base number density (cm^{-3})	$\langle n_{\rm e}\rangle^{\rm J\ base}$	$\mathbf{5 \times 10^7}$
Base temperature (K)	$T_{\rm e}^{\rm J\ base}$	$\mathbf{3 \times 10^{10}}$
	$\Theta_{\rm e}^{\rm J\ base}$	5.
Temperature slope	$s_{\rm T}$	**0.21**
κ-distribution index	κ	**5.5**
Magnetization parameter	$\sigma^{\rm J}$	0.01

Notes. The value of the parameter is given in bold if fitted. Otherwise, the value is fixed. See text for the definition of the parameters. For the temperatures, we also give the dimensionless electron temperature $\Theta_{\rm e} = kT_{\rm e}/(m_{\rm e}c^2)$. We note that the magnetic/gas pressure ratio defined by Eq. (6) is different from the standard plasma-β parameter. The latter is discussed in Eq. (12). We note that the total mass of the torus is $\approx 10^{-10}\,M_\odot$.

where $x_\alpha = (-7/4 + 8\kappa/5)^{-43/50}$, and ${}_2F_1(a, b; c; z)$ is the Gauss hypergeometric function. This function is computed by means of the implementation of Michel & Stoitsov (2008).

3. Spectra and images of the quiescent Sgr A*

We transport the synchrotron emission from the torus and jet described above by means of the general-relativistic open-source ray tracing code Gyoto[2] (Vincent et al. 2011). Null geodesics are traced backwards in coordinate time, from the distant observer towards the black hole. The radiative-transfer equation is integrated inside the torus and jet. We have made a resolution study to check that our choice of technical ray-tracing parameters, like the screen resolution and field of view of the observer, ensures a precision of <5% on the spectra. This study is briefly summarized in Appendix A.

Our torus+jet model is described by the set of 19 parameters described in Table 1. A complete study of the parameter space would be very long in terms of computing time, and not particularly interesting as we may converge to solutions that are unlikely to occur in reality. As a consequence, we prefer to rather investigate the parameter space in a rather small region around the best-fit values of the recent articles by Mościbrodzka & Falcke (2013), and Davelaar et al. (2018). Moreover, we simply fix those parameters that are already rather well constrained, or that are fully degenerate with other parameters. In this latter case, we choose values close to the best-fit numerical solutions available. The black hole mass and distance are fixed following Gravity Collaboration (2018b). We consider two illustrative values for the inclination (angle between the normal to the equatorial plane and the line of sight): either close to face-on, $i = 20°$, which is in agreement with the recent constraint from Gravity Collaboration (2018a), or close to edge-on, $i = 70°$. As mentioned above, the spin is likely to have a small impact on the results and is arbitrarily fixed to $a = 0$. The torus constant angular momentum scales the location of the torus center (where density and temperature are maximum), which we decide to fix arbitrarily at $r_{\rm cen} \approx 10\,GM\,c^{-2}$, leading to $\ell = 4\,GM\,c^{-3}$. The polytropic index is fixed to $k = 5/3$. The magnetization parameters are fixed to $\sigma^{\rm J} = 0.01$ in the jet and $\sigma^{\rm T} = 0.002$ in the torus. These values were chosen by requiring that the magnetic field be of the same order as that of the best fit of Davelaar et al. (2018), when the torus and jet number densities are set to the best-fit values of these authors. The jet inner and outer opening angles are fixed to values similar to that describing the jet sheath of Mościbrodzka & Falcke (2013). The opening angle of the jet has an overall increasing/decreasing effect on the spectrum that would be fully degenerate with the base number density. The jet base height is arbitrarily fixed to $2\,GM\,c^{-2}$ (coinciding with the Schwarzschild event horizon), while the bulk Lorentz factor is fixed to $\Gamma_j = 1.15$, approximately corresponding to the Keplerian velocity at the Schwarzschild innermost stable circular orbit. The remaining seven parameters (the central density, central temperature and inner radius of the torus, the base density and temperature of the jet, the temperature slope, and the κ index) are let free and are fitted to the spectral observations. The temperature slope and κ index have a strong impact on the spectrum slope in the radio and infrared region, respectively, meaning that their values can be rather easily constrained. There are therefore only five parameters that we scan in detail to find our best fits.

As we see in Fig. 3, the torus has a non-negligible impact on the spectrum only in the millimeter band. As a consequence, we divided our parameter space scanning into two easier sub-tasks: first we fitted a pure jet (with no torus) to the radio and infrared spectral data (removing the millimeter peak). Then we fixed the jet parameters at their values at the best fit of this search and fitted the torus parameters by fitting the full spectrum (from radio to infrared). This allows us to decrease the dimensions of the parameter space thus save computing time. We therefore considered one 2D grid (density, temperature) for the jet, and one separate 3D grid (density, temperature, inner radius) for the torus. We note that we fit our model to the spectral data only. The validity of the constraints on the radio image size and infrared spectral index are then checked a posteriori.

The left panel of Fig. 3 shows the best-fit spectra obtained for the two values of inclination considered here, $i = 20°$ and $i = 70°$. The fits are extremely good, with reduced chi-squared ≈ 1 for both inclinations. The best-fit parameters are listed in Table 1 for the $i = 20°$ case. Those of the $i = 70°$ case are the same except for the following: $r_{\rm in} = 6\,GM\,c^{-2}$, $\langle n_{\rm e}\rangle^{\rm T\ cen} = 8.7 \times 10^8$ cm^{-3}, $T_{\rm e}^{\rm T\ cen} = 6 \times 10^9$ K, $\langle n_{\rm e}\rangle^{\rm J\ base} = 7.5 \times 10^7$ cm^{-3}. It is interesting to compare the jet-base and torus-center values of the number density, temperature, and magnetic field to the best-fit GRMHD simulation of Davelaar et al. (2018). We checked that our best-fit values are within a maximum factor of ≈ 2.5 from that of these authors. This is a rather strong argument in favor of the robustness of both methods. It also shows that our

[2] See http://gyoto.obspm.fr/

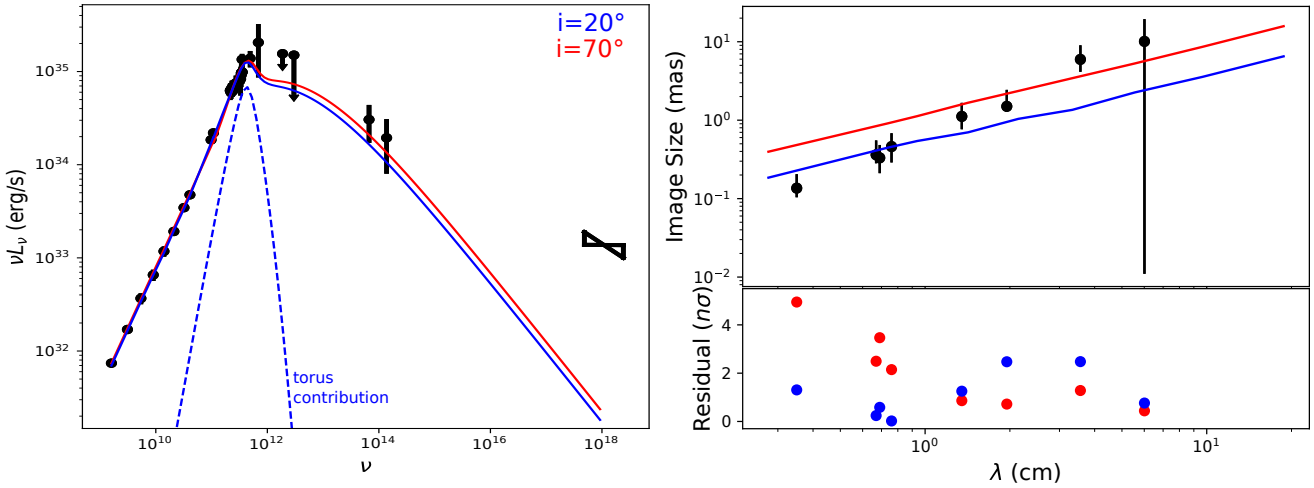

Fig. 3. *Left panel*: best-fit torus+jet quiescent spectrum at $i = 20°$ (blue, $\chi^2_{\rm red} = 0.54$, with the torus-only contribution dashed; it is very similar for both inclinations and therefore we represent only the $i = 20°$ case) and $i = 70°$ (red, $\chi^2_{\rm red} = 0.87$). The data are taken from Bower et al. (2015, all radio data except the four following points), Brinkerink et al. (2015, for the 2 points around 100 GHz), Liu et al. (2016, for the 492 GHz point), Marrone et al. (2006, for the 690 GHz point), von Fellenberg et al. (2018, for the far infrared upper limits), Witzel et al. (2018, or the mid infrared data), and Baganoff et al. (2001, for the X-ray bow-tie). We note that the X-ray data are not fitted as we do not take into account bremsstrahlung nor Comptonized emission. *Right panel*: corresponding image major axis at radio wavelengths (*upper panel*), with data from Bower et al. (2006). *Lower panel*: residual in units of σ.

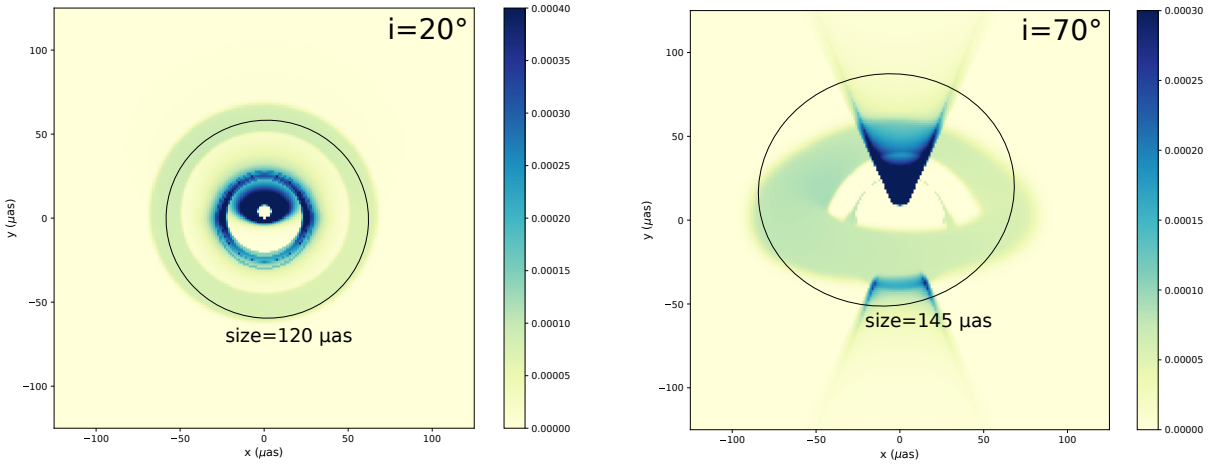

Fig. 4. Best-fit torus+jet image at 1.3 mm, as seen at inclination $i = 20°$ (*left panel*) and $i = 70°$ (*right panel*). The color bar is different for the two images to optimize the readability of each panel. It gives the value of the specific intensity in cgs units. The color hue is somewhat saturated to make it easier to see the fainter torus. As a consequence, the maximum value of the specific intensity is somewhat higher than the highest number of the color bars: 0.0015 for the *left panel*, and 0.001 for the *right panel*, in cgs units. The black ellipses are obtained by deriving the central moments of the images (see text for details) and give an estimate of the size of the emitting region, which is written explicitly in each panel.

much simpler analytic model captures the essential aspects of the physics at play. We also note the striking similarity between our best-fit nonthermal spectra and those of Yuan et al. (2003), developed for the very different context of RIAFs (see e.g., the recently updated Fig. 19 of Witzel et al. 2018). We consider that such comparisons are strong arguments in favor of the robustness of the simulations of Sgr A* accretion flow.

At this point, it is interesting to compute our best-fit plasma β parameter, as defined in the standard way of the ratio between the thermal-to-magnetic pressure ratio. We find

$$\beta = 8\pi \frac{\langle n_e \rangle k T_{\rm e}}{B^2} \approx 0.6, \quad (12)$$

which is valid both at the center of the torus and at the base of the jet. Our plasma is thus close to being fully magnetized (i.e., to $\beta = 1$). This value is comparable to the inner disk β of Ressler et al. (2017), as reported in their Fig. 1, lower-left panel.

Based on the recent detailed analysis of the infrared statistical properties of Sgr A* by Witzel et al. (2018), we can also discuss the value of our predicted infrared spectral index. Here, we define this index as the factor α such that the specific infrared flux follows $F_\nu \propto \nu^{-\alpha}$. This parameter is easily related to the κ index of our electron distribution through $\alpha = (\kappa - 2)/2$. With our best-fit value of $\kappa = 5.5$, the predicted spectral index of our model is thus $\alpha^{\rm predict} = 1.75$. The (dereddened) 2.2 μm luminosity of our $i = 20°$ best-fit model reaches $\nu L_\nu = 1.06{\times}10^{34}$ erg s^{-1}. Using Table 6 of Witzel et al. (2018), which gives the relation between dereddened and nondereddened fluxes of Sgr A*; this translates to a nondereddened flux of order 0.1 mJy. Using now Fig. 17 of Witzel et al. (2018), which gives the K-band spectral index as a function of the nondereddened flux, this translates

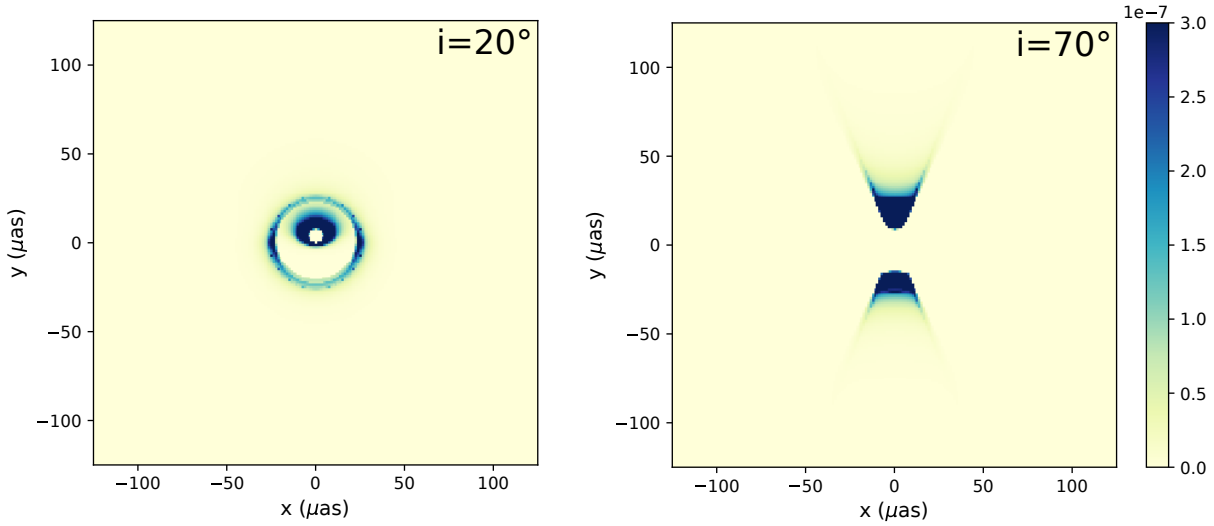

Fig. 5. Best-fit torus+jet image at 2.2 μm, as seen at inclination $i = 20°$ (*left panel*) and $i = 70°$ (*right panel*). The color bar is common to both panels and gives the values of specific intensity in cgs units. As in Fig. 4, the color hue is somewhat saturated for better visualization.

to a spectral index of the order of $\alpha^{\rm obs} = 1.8$, therefore very close to our predicted value. The slightly higher flux value at $i = 70°$ leads to similar conclusions. Thus, our best-fit models are coherent with the quiescent constraints on the spectral index of Sgr A*.

The third and final observable that we can use is the intrinsic radio sizes of Sgr A*. The right panel of Fig. 3 shows the predicted major axis size of our best-fit models for both inclinations compared to the data of Bower et al. (2006). The major axis of the image is computed from its central moments. We briefly reiterate this formalism in Appendix B. The right panel of Fig. 3 shows that our $i = 20°$ best-fit model is always at $<2.5\sigma$ from the 0.35 to 6 cm data of Bower et al. (2006), which gives a reasonable agreement over this range. However, our model predicts that the size evolves like λ^{γ}, where $\gamma \approx 0.8$, which is too shallow with respect to the constraint of Bower et al. (2006), who find that $\gamma^{\rm obs} \approx 1.6$. This causes our model to overpredict the size of the image at lower wavelengths, as we see below. We note that the centimeter-size behavior of our model is very similar to that depicted in Fig. 9 of Davelaar et al. (2018), again showing the ability of our simple description to lead to the same conclusions as the most sophisticated GRMHD simulations to date. Let us stress that the slope of the curve in the right panel of Fig. 3 is only weakly dependent on the jet parameters. Davelaar et al. (2018) and Chael et al. (2018) have shown that the size of the centimeter-emitting region is sensitive to the electron distribution function, meaning that the shallow slope that we get might be linked to our choice of purely κ-distribution electrons.

Doeleman et al. (2008) gave a constraint on the intrinsic diameter of Sgr A* at 1.3 mm of 37^{+16}_{-10} μas (3σ) based on a Gaussian fit. It is therefore particularly interesting to examine the prediction of our model at this specific EHT wavelength. Figure 4 shows the 1.3 mm best-fit image of our model for both inclinations. It shows that our predicted 1.3 mm size (as computed from image moments) is larger by a factor of approximately three at $i = 20°$ and approximately four at $i = 70°$, as compared to the Doeleman et al. (2008) constraint. This is mainly due to the presence of the faint extended torus, while our images also show prominent features at the $\lesssim$40 μas scale. The time-evolving GRMHD model of Davelaar et al. (2018) leads, here again, to very similar results. The millimeter constraint on the emitting-region size reported above is valid assuming a circular

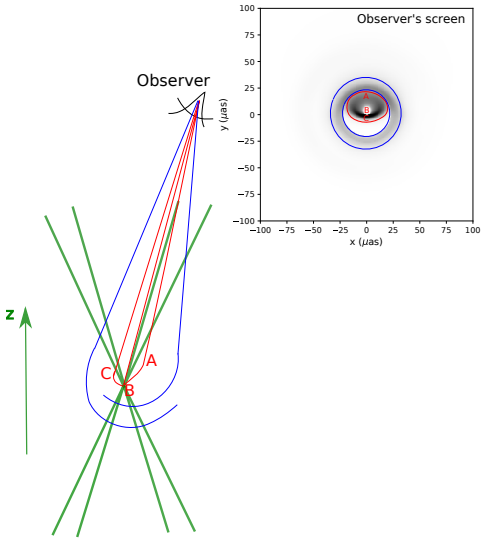

Fig. 6. Green contours: scheme of the jet sheath on both parts ($z > 0$ and $z < 0$) of the black hole. The observer is at $i = 20°$ at the *top* of the figure, with the observation screen represented at the top right. It is identical to the left panel of Fig. 5. Two regions are highlighted in red and blue. The red part is the primary image of the regions close to the $z > 0$ base of the jet. Three examples of geodesics, ray-traced backwards in time from the screen of the observer, A, B, and C, are represented on the scheme, all of them ending their trajectory inside the black hole. Their end points on the screen of the observer are labeled. Geodesic C carries more flux, because it has visited regions very close to the base of the jet. While geodesic B, falling (backwards) straight into the black hole, carries no flux. The toroidal blue region on the screen of the observer is the secondary image of the jet, due to photons that are strongly bent in the regions close to the $z < 0$ base of the jet, before reaching the far-away observer. Two such strongly bent geodesics are depicted in blue on the scheme. This structure can therefore be seen as the Einstein ring of the $z < 0$ base of the jet.

Gaussian model for the source. A thick-ring model leads to an outer diameter intrinsic source size of $\approx$80 μas, hence a factor of about 1.5 smaller than our face-on prediction. The constraint of Doeleman et al. (2008) is therefore only the first word on a nascent topic. In particular, this constraint is only valid in the projected direction of the baseline on sky, meaning that a

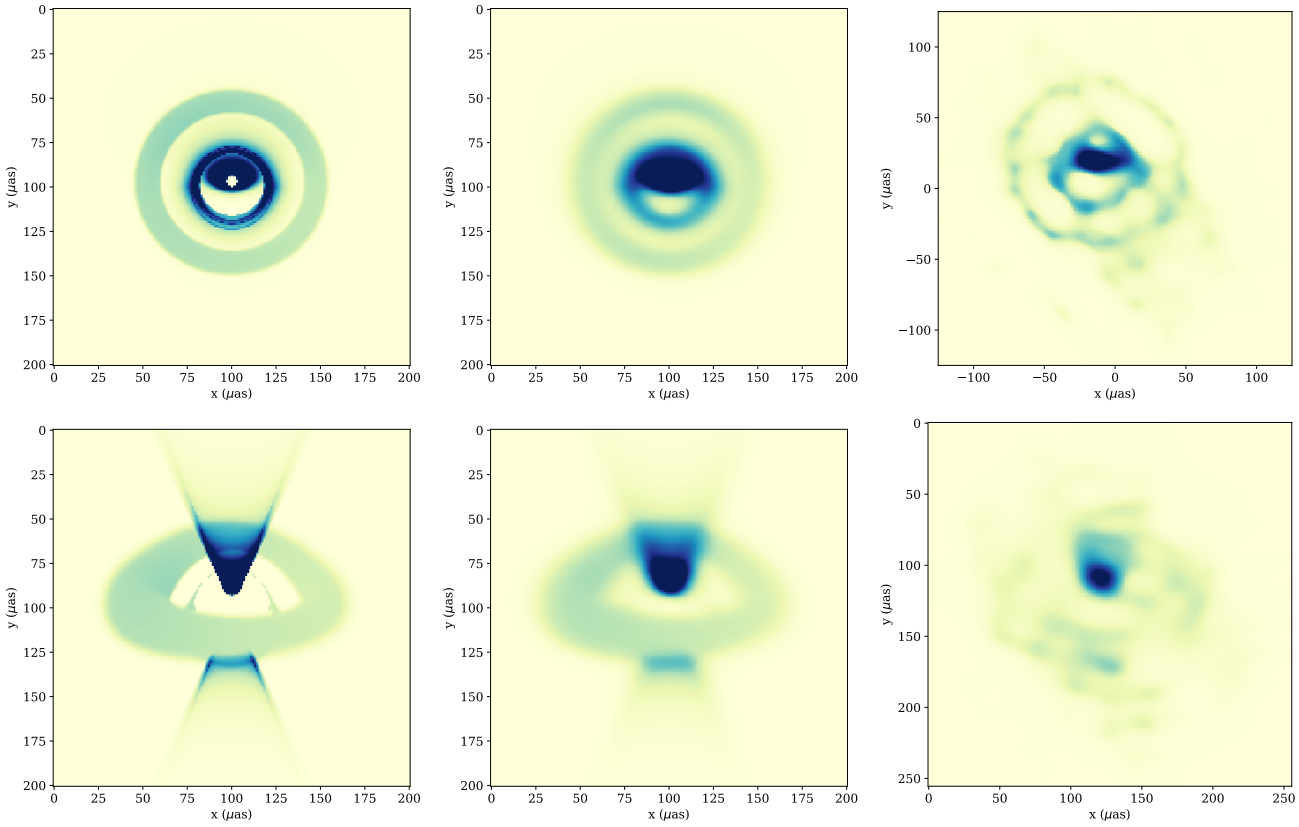

Fig. 7. Example of model images reconstruction with the synthetic EHT array. For display purposes color maps saturate at 0.001 Jy px^{-1}. *Left column*: original synthetic images generated with our model (same as Fig. 4). *Middle column*: model images as processed by the interstellar scattering screen (Johnson et al. 2018). *Right column*: MEM reconstruction of images, observed by a synthetic EHT 2017 array (Chael et al. 2016). Fitting an elliptical Gaussian component to images we find a characteristic size [major axis, minor axis] of [97,72] μas for the *top row* image and [100,89] μas for the *bottom row* image.

complex geometry (like we have here with a thick disk and a jet), with an intrinsic size varying a lot with the angle on sky, might be too broadly described by this single number only. Therefore, we consider that our 1.3 mm flux repartition is in reasonable agreement with the data. It is likely that the near-future EHT data will allow for the geometry of the inner accretion flow to be more precisely constrained, allowing to further refine the modeling part.

Figure 4 shows that the 1.3 mm image is due to a mix of contributions from the torus and the jet. At radio wavelengths ($<10^{11}$ Hz), the jet completely dominates the spectrum, as emission primarily comes from large scales. Our model is also fully dominated by the jet for near-infrared frequencies and above, as illustrated in Fig. 5, which shows the best-fit 2.2 μm images at both inclinations. This feature is in reasonable agreement with the near-infrared images of Davelaar et al. (2018). However, this disagrees with the results of Ressler et al. (2017) who find that the disk dominates at all frequencies above the millimeter peak. This difference is certainly due to the different electron temperatures in the various models. In particular, Ressler et al. (2017) report hot spots of high electron temperature in the disk that are obviously not present in our simple setup. These hot spots lead to a high near-infrared flux, which would not agree with the faintest quiescent level of Sgr A*.

Although the right panel of Fig. 5, showing the edge-on ray-traced image of a jet, is easy to interpret, it is likely that the left panel, showing the same scenery from a face-on view, is more complicated. Figure 6 is an attempt to explain this image, and shows that the annular structure is actually the Einstein ring of the $z < 0$ base of the jet.

4. Reconstructing synthetic data with the EHT array

An important question to ask is whether salient features of the near-horizon emission region of Sgr A*, which we are parametrizing with analytic geometric models, could actually be observed by an instrument such as the EHT. The question concerns not only the instrument resolution, but also inherent limitations of the imaging from sparsely sampled Fourier domain data and the use of a strongly inhomogeneous array of telescopes, both being traits of VLBI in general and EHT in particular. One of the limitations is a low dynamic range of VLBI synthesis images; see for example Braun (2013). For a multicomponent source this could result in the inability of the EHT observations to reliably detect a weaker-flux component, such as a faint torus in the presence of a bright jet.

We investigate this issue by generating synthetic EHT observations of the images shown in Fig. 4 and subsequently attempting to reconstruct the images from sparsely sampled data. Synthetic observations and image reconstructions are generated using the freely available `eht-imaging` library[3]. A Maximum Entropy Method (MEM), implemented in `eht-imaging`, was used for the image reconstruction; see Chael et al. (2016). The simulated observations fold in characteristic sensitivities of the EHT telescopes, and effects such as thermal noise contamination, rapid atmospheric phase variation, and dependence of sensitivity on source elevation. The EHT 2017 array was used, with optimal coverage in the Fourier domain. A static source model

[3] https://github.com/achael/eht-imaging

(i.e., single image) was assumed, which is a significant simplification, as time variability on timescales as short as minutes is expected for Sgr A*. No mitigation of scattering, subdominant for 1.3 mm wavelength, was employed.

Event Horizon Telescope reconstruction results are shown in Fig. 7. They show that the salient features of the models persist in the reconstructed images. In particular, a wide region of weak emission, corresponding to the faint torus, is present in the reconstructed images. This successful reconstruction of the model images allows us to hope that similar features of the realistic Sgr A* accretion/ejection flow could be successfully revealed in EHT images. If so, simple geometric models such as ours could help in interpreting future data and extracting relevant parameters, such as, in the present case, the inclination angle. Figure 7 indeed shows that the reconstructed image is clearly dependent on this important parameter.

5. Conclusion and perspectives

Here we present a simple analytic model of the quiescent-state emission of Sgr A*, made from the combination of a compact torus and a large-scale jet sheath. Our model allows to fit the multi-wavelength spectral data of Sgr A* very well, as illustrated in the left panel of Fig. 3. The size of the radio/millimeter emitting region is in reasonable agreement with observed constraints, as illustrated in the right panel of Fig. 3 and in the discussion accompanying Fig. 4. Figure 7 demonstrates that salient disk/jet features of our model images persist when synthetic data are "observed" and reconstructed using a numerical model of the EHT array, and that these features are sensitive to inclination.

It is interesting that our model, inspired by the recent work of Davelaar et al. (2018), leads to best-fit parameters very close to those found in the GRMHD simulations of these authors. We believe that this is a nice illustration of the interest of simple analytic models: they are able to reproduce the outputs of costly numerical simulations. It is also interesting that our spectral prediction is indistinguishable from the predictions of Yuan et al. (2003), who use a different analytic description of the surroundings of Sgr A*. This is a good argument that the theoretical descriptions of Sgr A* are robust in their predictions.

We consider that our model is a practical testbed for the study of various aspects of the physics of Sgr A*. We hope that this model will be useful for other authors; we describe all steps necessary to reproduce our results in Appendix C. In the near future, we aim at using this model to analyze and interpret the data from GRAVITY, EHT, and possibly other millimeter-range VLBI observations.

Acknowledgements. FHV acknowledges fruitful inputs from T. Bronzwaer, J. Davelaar and G. Witzel. FHV acknowledges many interesting discussions at the *Central Arcsecond* conference in Ringberg (Nov. 2018), and would like to thank T. Do, H. Falcke, S. von Fellenberg, D. Wang, and the organizers of the conference. FHV acknowledges interesting email exchanges with F. Yuan. MAA acknowledges the Polish NCN grant 2015/19/B/ST9/01099 and the Czech Science Foundation grant No. 17-16287S which supported his visits to the Paris Observatory and to Harvard University; Harvard's Black Hole Initiative support is also acknowledged. AAZ has been supported in part by the Polish National Science Centre grants 2013/10/M/ST9/00729 and 2015/18/A/ST9/00746.

References

Alberdi, A., Lara, L., Marcaide, J. M., et al. 1993, A&A, 277, L1
Baganoff, F. K., Bautz, M. W., Brandt, W. N., et al. 2001, Nature, 413, 45
Bietenholz, M. F., Bartel, N., & Rupen, M. P. 2000, ApJ, 532, 895
Birchfield, S. 2018, Image Processing and Analysis (Boston: CENGAGE Learning)
Blandford, R. D., & Königl, A. 1979, ApJ, 232, 34
Bower, G. C., Goss, W. M., Falcke, H., Backer, D. C., & Lithwick, Y. 2006, ApJ, 648, L127
Bower, G. C., Markoff, S., Brunthaler, A., et al. 2014, ApJ, 790, 1
Bower, G. C., Markoff, S., Dexter, J., et al. 2015, ApJ, 802, 69
Braun, R. 2013, A&A, 551, A91
Brinkerink, C. D., Falcke, H., Law, C. J., et al. 2015, A&A, 576, A41
Broderick, A. E., Fish, V. L., Johnson, M. D., et al. 2016, ApJ, 820, 137
Chael, A. A., Johnson, M. D., Narayan, R., et al. 2016, ApJ, 829, 11
Chael, A., Rowan, M., Narayan, R., Johnson, M., & Sironi, L. 2018, MNRAS, 478, 5209
Davelaar, J., Mościbrodzka, M., Bronzwaer, T., & Falcke, H. 2018, A&A, 612, A34
Dexter, J., Agol, E., Fragile, P. C., & McKinney, J. C. 2010, ApJ, 717, 1092
Dibi, S., Drappeau, S., Fragile, P. C., Markoff, S., & Dexter, J. 2012, MNRAS, 426, 1928
Dodds-Eden, K., Gillessen, S., Fritz, T. K., et al. 2011, ApJ, 728, 37
Doeleman, S. S., Weintroub, J., Rogers, A. E. E., et al. 2008, Nature, 455, 78
Doeleman, S., Agol, E., & Backer, D. 2009, Astronomy, 2010, 68
Falcke, H., & Markoff, S. 2000, A&A, 362, 113
Falcke, H., Mannheim, K., & Biermann, P. L. 1993, A&A, 278, L1
Falcke, H., Melia, F., & Agol, E. 2000a, ApJ, 528, L13
Falcke, H., Nagar, N. M., Wilson, A. S., & Ulvestad, J. S. 2000b, ApJ, 542, 197
Falcke, H., Markoff, S., & Bower, G. C. 2009, A&A, 496, 77
Genzel, R., Eisenhauer, F., & Gillessen, S. 2010, Rev. Mod. Phys., 82, 3121
Ghez, A. M., Salim, S., Weinberg, N. N., et al. 2008, ApJ, 689, 1044
Gillessen, S., Eisenhauer, F., Trippe, S., et al. 2009, ApJ, 692, 1075
Gold, R., McKinney, J. C., Johnson, M. D., & Doeleman, S. S. 2017, ApJ, 837, 180
Gravity Collaboration (Abuter, R., et al.) 2017, A&A, 602, A94
Gravity Collaboration (Abuter, R., et al.) 2018a, A&A, 618, L10
Gravity Collaboration (Abuter, R., et al.) 2018b, A&A, 615, L15
Issaoun, S., Johnson, M. D., Blackburn, L., et al. 2019, ApJ, 871, 30
Jiménez-Rosales, A., & Dexter, J. 2018, MNRAS, 478, 1875
Johnson, M. D. 2016, ApJ, 833, 74
Johnson, M. D., Narayan, R., Psaltis, D., et al. 2018, ApJ, 865, 104
Komissarov, S. S. 2006, MNRAS, 368, 993
Lamy, F., Gourgoulhon, E., Paumard, T., & Vincent, F. H. 2018, Class. Quant. Grav., 35, 115009
Liu, H. B., Wright, M. C. H., Zhao, J.-H., et al. 2016, A&A, 593, A44
Markoff, S., Falcke, H., Yuan, F., & Biermann, P. L. 2001, A&A, 379, L13
Marrone, D. P., Moran, J. M., Zhao, J.-H., & Rao, R. 2006, J. Phys. Conf. Ser., 54, 354
McConnell, M. L., Zdziarski, A. A., Bennett, K., et al. 2002, ApJ, 572, 984
Michel, N., & Stoitsov, M. V. 2008, Comput. Phys. Commun., 178, 535
Mościbrodzka, M., & Falcke, H. 2013, A&A, 559, L3
Mościbrodzka, M., Gammie, C. F., Dolence, J. C., Shiokawa, H., & Leung, P. K. 2009, ApJ, 706, 497
Narayan, R., Yi, I., & Mahadevan, R. 1995, Nature, 374, 623
Özel, F., Psaltis, D., & Narayan, R. 2000, ApJ, 541, 234
Pandya, A., Zhang, Z., Chandra, M., & Gammie, C. F. 2016, ApJ, 822, 34
Paumard, T., Vincent, F. H., Straub, O., & Lamy, F. 2019, Gyoto 1.3.1 DOI 10.5281/zenodo.2547541
Quataert, E. 2002, ApJ, 575, 855
Rees, M. J. 1982, in The Galactic Center, eds. G. R. Riegler, & R. D. Blandford, Am. Inst. Phys. Conf. Ser., 83, 166
Ressler, S. M., Tchekhovskoy, A., Quataert, E., & Gammie, C. F. 2017, MNRAS, 467, 3604
Shcherbakov, R. V., Penna, R. F., & McKinney, J. C. 2012, ApJ, 755, 133
Straub, O., Vincent, F. H., Abramowicz, M. A., Gourgoulhon, E., & Paumard, T. 2012, A&A, 543, A83
Vincent, F. H., Paumard, T., Gourgoulhon, E., & Perrin, G. 2011, Class. Quant. Grav., 28, 225011
Vincent, F. H., Yan, W., Straub, O., Zdziarski, A. A., & Abramowicz, M. A. 2015, A&A, 574, A48
Vincent, F. H., Gourgoulhon, E., Herdeiro, C., & Radu, E. 2016a, Phys. Rev. D, 94, 084045
Vincent, F. H., Meliani, Z., Grandclément, P., Gourgoulhon, E., & Straub, O. 2016b, Class. Quant. Grav., 33, 105015
von Fellenberg, S. D., Gillessen, S., Graciá-Carpio, J., et al. 2018, ApJ, 862, 129
Wang, Q. D., Nowak, M. A., Markoff, S. B., et al. 2013, Science, 341, 981
Wardziński, G., & Zdziarski, A. A. 2000, MNRAS, 314, 183
Witzel, G., Martinez, G., Hora, J., et al. 2018, ApJ, 863, 15
Yuan, F., & Narayan, R. 2014, ARA&A, 52, 529
Yuan, F., Markoff, S., & Falcke, H. 2002, A&A, 383, 854
Yuan, F., Quataert, E., & Narayan, R. 2003, ApJ, 598, 301

Appendix A: Resolution study

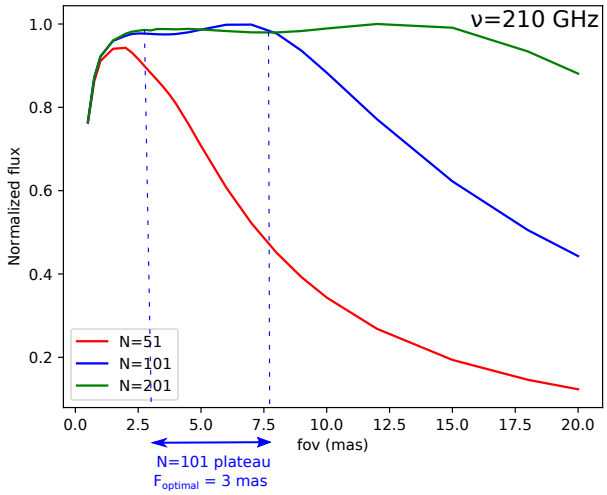

Fig. A.1. Evolution of the normalized ray-traced flux at $\nu = 210$ GHz with increasing field of view for three values of screen resolution, $N = 51$ (red), $N = 101$ (blue), and $N = 201$ (green). The optimal value of field of view for a given resolution is the beginning of the plateau-phase of the curve (see text for details). The plateaus of the $N = 101$ and $N = 201$ curves are identical to within 0.1%, which shows that $N = 101$ is the smallest resolution that ensures accurate flux values, associated to $F = 3$ mas.

The emitting part of the jet in the radio range can extend to large distances, allowing one to consider a large field of view for the ray tracing computation. Here, we investigate the resolution of the Gyoto screen (i.e., the number of pixels along one dimension, labeled N) needed to obtain a precise value of the observed flux. We want to determine the optimal pair of field of view F and resolution N. To do so, we study the evolution of the normalized flux with the field of view, for various resolutions and for a set of wavelengths. The overall behavior of these curves is easy to understand. For a given resolution, if the field of view is too small, the predicted flux is also too small because a portion of the emitting region leaks out of the field of view. If the field of view is too big, the predicted flux will also be too small, because the emitting region is diluted (at the limit of a field of view 4π steradian, the emitting region would be so small that the image would be completely black, leading to zero flux). Thus, the curve showing the evolution of the flux as a function of the field of view first increases with the field of view, then stabilizes to form a plateau, and finally decreases. We select our (N, F) pairs by imposing that the plateaus of the curves corresponding to N and to $2N$ are equal to within <5%. For the minimal N satisfying this condition, we choose the smallest value of F within the plateau. A smaller F will lead to a smaller computing time (because the region to trace is smaller), meaning that this is the optimal choice in terms of both precision and computing time. Figure A.1 illustrates this procedure for the particular case of $\nu = 210$ GHz. This figure shows that the plateau fluxes corresponding to the $N = 101$ and $N = 201$ curves are equal to within 0.1%, while the $N = 51$ plateau is 6% off and is therefore rejected. Table A.1 gives the various (N, F) used in this article as a function of the observed frequency.

Table A.1. Pairs of resolution N and corresponding field of view F used for the $i = 20°$ simulations of Sect. 3.

ν (Hz)	$(N, F(\text{mas}))$
1.6×10^9	$(101, 30)$
3.1×10^9	$(101, 15)$
5.4×10^9	$(101, 10)$
9×10^9	$(101, 5)$
1.4×10^{10}	$(101, 5)$
2.1×10^{10}	$(101, 3)$
3.2×10^{10}	$(101, 3)$
4.09×10^{10}	$(101, 2.5)$
1.08×10^{11}	$(201, 1)$
$>1.1 \times 10^{11}$	$(201, 0.5)$

Appendix B: Image moments

Let $I(x, y)$ be a 2D image labeled by a Cartesian grid (x, y). The central moment of order $p + q$ of image I is the quantity

$$\mu_{pq} = \sum_x \sum_y (x - \bar{x})^p (y - \bar{y})^q \, I(x, y), \tag{B.1}$$

where $(\bar{x}, \bar{y})$ is the centroid of the $I(x, y)$ distribution, that is,

$$\bar{x} = \frac{\sum_x \sum_y x \, I(x, y)}{\sum_x \sum_y I(x, y)}, \tag{B.2}$$

and similarly for $\bar{y}$.

The major axis of the best-fitting ellipse adjusted to the distribution of $I(x, y)$ in the image is then given by (Birchfield 2018)

$$L = 2 \sqrt{2 \frac{\mu_{20} + \mu_{02} + \sqrt{(\mu_{20} - \mu_{02})^2 + 4\mu_{11}^2}}{\mu_{00}}}, \tag{B.3}$$

while the orientation of the ellipse with respect to the Cartesian grid (x, y) is

$$\tan 2\theta = \frac{2\mu_{11}}{\mu_{20} - \mu_{02}}. \tag{B.4}$$

The size-fitting ellipses of Fig. 4 are computed using these formulas, as implemented in the `cv2` Python package.

Appendix C: Using Gyoto to generate spectra and images

The code developed for this paper is part of Gyoto 1.3.1 (Paumard et al. 2019)[4]. Gyoto is packaged for Debian GNU/Linux and its derivatives including Ubuntu and this version will be part of the next version of these operating systems to be released in 2019. The installation steps are detailed in the file INSTALL.Gyoto.md (skipping section 0: the pre-compiled versions of Gyoto do not contain the very recent new developments presented in this article).

The input file Gyoto/doc/examples/example-jet.xml gives the jet-only best-fit model for the $i = 20^\circ$ case discussed in Sect. 3. The file Gyoto/doc/examples/example-torusjet.xml gives the torus+jet best-fit model, that is, the model used to generate the face-on spectrum and image of Figs. 3 and 4. The xml files provided have parameters such that they allow an accurate computation of the spectrum in the 10^{11}–10^{18} Hz range. Lower frequencies need higher resolution and longer computing time; see Appendix A.

The Python scripts Gyoto/doc/examples/plot-Spectrum.py and Gyoto/doc/examples/plot-Image.py allow us to straightforwardly generate spectra (together with the latest observed data) and images (together with the best-fitting image-moment ellipse), just as in our Figs. 3 and 4.

We thus provide all the software needed to obtain the results presented in this article.

Interested people are very welcome to contact the Gyoto developers at frederic.vincent@obspm.fr, thibaut.paumard@obspm.fr for help.

[4] Also available at https://github.com/gyoto/Gyoto/tree/1.3.1.